

Statistical transition to turbulence in plane channel flow

Sébastien Gomé* and Laurette S. Tuckerman†

*Laboratoire de Physique et Mécanique des Milieux Hétérogènes (PMMH), CNRS, ESPCI Paris,
PSL Research University, Sorbonne Université, Université Paris Diderot, Paris 75005, France*

Dwight Barkley‡

Mathematics Institute, University of Warwick, Coventry CV4 7AL, United Kingdom

(Dated: September 11, 2022)

Intermittent turbulent-laminar patterns characterize the transition to turbulence in pipe, plane Couette and plane channel flows. The time evolution of turbulent-laminar bands in plane channel flow is studied via direct numerical simulations using the parallel pseudospectral code ChannelFlow in a narrow computational domain tilted by 24° with respect to the streamwise direction. Mutual interactions between bands are studied through their propagation velocities. Profiles show that the flow surrounding isolated turbulent bands returns to the laminar base flow over large distances. Depending on the Reynolds number, a turbulent band can either decay to laminar flow or split into two bands. As with past studies of other wall-bounded shear flows, in most cases survival probability distributions are found to be exponential for both decay and splitting, indicating that the processes are memoryless. Statistically estimated mean lifetimes for decay and splitting are plotted as a function of the Reynolds number and lead to the estimation of a critical Reynolds number $Re_{\text{cross}} \simeq 950$, where decay and splitting lifetimes cross at greater than 10^6 advective time units. The processes of splitting and decay are also examined through analysis of their Fourier spectra. The dynamics of large-scale spectral components seem to statistically follow the same pathway during the splitting of a turbulent band and may be considered as precursors of splitting.

* sebastien.gome@espci.fr

† laurette.tuckerman@espci.fr

‡ D.Barkley@warwick.ac.uk

I. INTRODUCTION

The route to turbulence in many wall-bounded shear flows involves intermittent laminar-turbulent patterns that evolve on vast space and time scales ([1] and references therein). These states have received much attention over the years, both because of their intrinsic fascination and also because of their fundamental connection to critical phenomena associated with the onset of sustained subcritical turbulent flows. Below a critical Reynolds number, intermittent turbulence exists only transiently – inevitably reverting to laminar flow, possibly after some very long time. Just above the critical Reynolds number, turbulence becomes sustained in the form of intermittent laminar-turbulent patterns.

Flow geometry, specifically the number of unconstrained directions, plays an important role in these patterns. In flows with one unconstrained direction, large-scale turbulent-laminar intermittency can manifest itself only in that direction. Pipe flow is the classic example of such a system [2], but other examples are variants such as duct flow [3] and annular pipe flow [4], and also constrained Couette flow between circular cylinders where the height and gap are both much smaller than the circumference [5]. In terms of large-scale phenomena, these systems are viewed as one dimensional. Turbulent-laminar intermittency takes the comparatively simple form of localized turbulent patches, commonly referred to as puffs, interspersed within laminar flow [6–8]. In this case much progress has been made in understanding the localization of puffs and the critical phenomena associated with them [5, 9–13].

In flow geometries with one confined and two extended directions, turbulent-laminar intermittency takes a more complex form that is dominated by turbulent bands which are oriented obliquely to the flow direction. Examples of such flows are Taylor-Couette flow [14–20], plane Couette flow [20, 21], plane channel flow [22–24], and a free-slip version of plane Couette flow called Waleffe flow [25, 26]. In terms of large-scale phenomena, one views these systems as two dimensional. Understanding the transition scenario in these systems is complicated by the increased richness of the phenomena they exhibit and also by the experimental and computational challenges involved in studying systems with two directions substantially larger than the wall separation. So large are the required dimensions that is only for a truncated model of Waleffe flow that it has been possible to verify that the transition to turbulence is of the universality class of two-dimensional directed percolation [27].

Between the one-dimensional and fully two-dimensional cases are the numerically obtainable restrictions of planar flows to long, but narrow, periodic domains tilted with respect to the flow direction. These domains restrict turbulent bands to a specified angle. They have only one long spatial direction, thereby limiting the allowed large-scale variation to one dimension, but they permit the flow along the narrow direction, flow that is necessary for supporting turbulent bands in planar shear flows. Such computational domains were originally proposed as minimal computational units to capture and understand the oblique turbulent bands observed in planar flows [28]. Tilted computational domains have subsequently been used in numerous studies of transitional wall-bounded flows, notably plane Couette flow [5, 29–31] as well as a survey of plane channel flow [32]. Shi, Avila & Hof [33] used simulations in a tilted domain to measure decay and splitting lifetimes in plane Couette flow and it is this approach that we apply here to plane channel flow.

We mention two important points concerning the relevance of turbulent bands in narrow tilted domains to those in plane channel flow in large domains. The first is that a regime in transitional channel flow has been discovered at Reynolds numbers lower than those studied here in which turbulent bands elongate at their downstream end while they retract from their upstream end [18, 34–36]. This one-sided regime plays an important role in the full scenario of transition for channel flow [37]. Such bands of long but finite length are excluded in narrow tilted domains. The second point is that critical Reynolds numbers obtained in narrow tilted domains [33, 38] have been found to agree closely with transition thresholds found in the full planar setting [21, 27, 39, 40] in both plane Couette flow and in stress-free Waleffe flow. We will return to both of these points in Sec. VI.

Here we study the onset of turbulent channel flow using narrow tilted domains. We are particularly focused on establishing the time scales and Reynolds numbers associated with the splitting and decay processes.

II. NUMERICAL PROCEDURE AND CHOICE OF DIMENSIONS

Plane channel flow is generated by imposing a bulk velocity on flow between two parallel rigid plates. The length scales are nondimensionalized by the half-gap h between the plates and velocities by $3U_{\text{bulk}}/2$. This velocity scale is the center-line velocity of parabolic channel flow with bulk velocity U_{bulk} and stationary walls. The Reynolds number is then defined to be $Re = 3U_{\text{bulk}}h/(2\nu)$.

The computational domain used in this study is tilted with respect to the streamwise direction, as illustrated in Fig. 1. The domain is a narrow periodic box with the narrow dimension (labelled by the x coordinate) aligned along the turbulent band. The long dimension of the domain (labelled by the z coordinate) is orthogonal to the bands, i.e. it is aligned with the pattern wavevector. The relationship between streamwise-spanwise coordinates and (x, z)

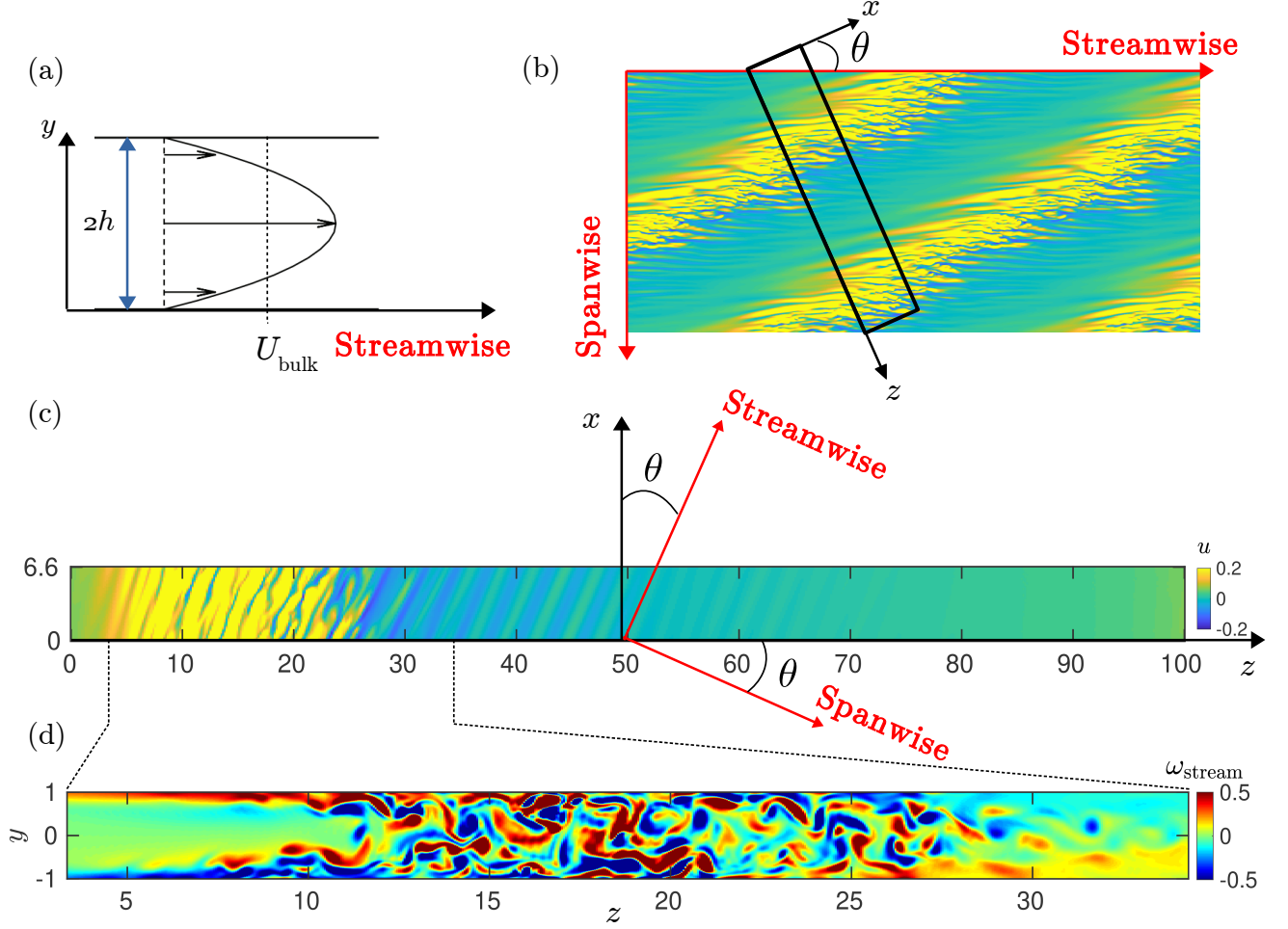


FIG. 1: (a) Sketch of the laminar profile. (b) Visualization of bands in a 240×108 streamwise-spanwise domain, where colors indicate the streamwise velocity. The numerical domain (black box) is tilted with an angle θ relative to the streamwise direction. (c) Structure of a turbulent-laminar pattern in the oblique (x, z) domain at $Re = 1200$. Streamwise and spanwise directions are indicated in red. The velocity in the x direction is shown here, at the plane $y = -0.8$. The band spans from $z \simeq 5$ to $z \simeq 25$. Then, from $z \simeq 25$ to $z \simeq 65$, the flow shows weak straight streaks, oriented in the streamwise direction, making up the turbulent-laminar interface. Finally, the flow is quasi-laminar from $z \simeq 70$ to $z \simeq 5$. (d) Streamwise vorticity (deviation from laminar vorticity) in a stretched (y, z) plane in the region surrounding the band ($z = 3$ to 35).

coordinates is:

$$\mathbf{e}_{\text{streamwise}} = \cos \theta \mathbf{e}_x + \sin \theta \mathbf{e}_z \quad (1a)$$

$$\mathbf{e}_{\text{spanwise}} = -\sin \theta \mathbf{e}_x + \cos \theta \mathbf{e}_z \quad (1b)$$

The wall-normal coordinate is denoted y and is independent of the tilt.

The angle in this study is fixed at $\theta = 24^\circ$, as has been used extensively in the past. The tilt angle of the domain imposes a fixed angle on turbulent bands. The narrowness of the computational domain (in the x direction) means that simulations prohibit any large-scale variation along turbulent bands, effectively simulating infinitely long bands. These restrictions of a tilted domain have both advantages and disadvantages for simulations of transitional turbulence. We return to this in the discussion.

We have carried out direct numerical simulations (DNS) using the parallelized pseudospectral C++-code ChannelFlow [41]. This code simulates the incompressible Navier-Stokes equations in a periodic channel by employing a Fourier-Chebyshev spatial discretization, fourth-order semi-implicit backwards-differentiation time stepping, and an influence matrix method with Chebyshev tau correction on the primitive-variables formulation. The velocity field

is decomposed into a parabolic base flow and a deviation, $\mathbf{U} = \mathbf{U}_{\text{base}} + \mathbf{u}$, where the deviation field has zero flux. Simulating in the tilted domain gives velocity components $\mathbf{u} = (u, v, w)$ aligned with the oblique coordinates (x, y, z) .

Most of the simulations presented have been carried out in a domain with dimensions $(L_x, L_y, L_z) = (6.6, 2, 100)$. The numerical resolution is $(N_x, N_y, N_z) = (84, 64, 1250)$, which both ensures that $\Delta x = \Delta z \simeq 0.08$ and that Δy varies from $\Delta y = \cos(31\pi/64) = 0.05$ at $y = 0$ to $\Delta y = 1 - \cos(\pi/64) = 0.001$ at $y = \pm 1$. This resolution has been shown to be sufficient to simulate small turbulent scales at low Reynolds numbers (Kim *et al.* [42], Tsukahara *et al.* for $Re = 1370$ [22]).

In the Fourier-Chebyshev discretization the deviation velocity is expressed as:

$$\mathbf{u} = \sum_{-N_x/2+1}^{N_x/2} \sum_{-N_z/2+1}^{N_z/2} \sum_0^{N_y} \hat{\mathbf{u}}_{m_x, m_y, m_z} e^{i(k_x m_x x + k_z m_z z)} T_{m_y}(y) \quad (2)$$

where $k_x = 2\pi/L_x$, $k_z = 2\pi/L_z$, $\hat{\mathbf{u}}_{m_x, m_y, m_z}$ are the Fourier-Chebyshev coefficients, and $T_{m_y}(y)$ are the Chebyshev polynomials.

The structure of a typical turbulent band in this domain is shown on Fig. 1. A series of straight periodic streaks is visible at the downstream interface between the turbulent band and the laminar flow, whereas the upstream interface is much sharper. Streaks are visible here as streamwise structures modulated along the spanwise direction. They are wavy at the core of the turbulent zone, in accordance with the self-sustaining process of transitional turbulence [25].

Our choice for the standard domain dimensions, $(L_x, L_y, L_z) = (6.6, 2, 100)$, is dictated as follows: $L_y = 2$ is fixed by non-dimensionalization. The choice of the short dimension L_x is dictated by the natural streak wavenumber. In plane Couette flow, this was found to be approximately $L_{x, \text{Couette}} = 10 = 4/\sin 24^\circ$ [43], and widely used since [28, 33]. Chantry *et al.* showed that the correspondence between length scales in plane Couette and plane channel flows is $h_{\text{Poiseuille}} \simeq 1.5h_{\text{Couette}}$ [26], leading to an optimal short dimension in a 24° box of $L_{x, \text{Poiseuille}} = 6.6$. $L_z = 100$ is chosen to be sufficiently large that periodicity in the z -direction does not have a significant effect on the turbulent band dynamics, as we will see in the next section.

III. BAND VELOCITY AND INTERACTION LENGTH

As in pipe flow [9, 10, 13], bands in channel flow interact when sufficiently close and this can affect the quantities we seek to measure. For example, in a one-dimensional directed percolation model [44, p. 167], the time scales observed for decay and splitting increase strongly with the inter-band distance, while the critical point increases weakly. We wish to choose the length L_z of our domain to be the minimal distance above which bands can be considered to be isolated.

Unlike their counterparts in plane Couette flow, turbulent bands in plane channel flow are not stationary relative to the bulk velocity U_{bulk} . Bands move either faster or slower than the bulk velocity, depending on the Reynolds number [32]. One important way the interaction between bands manifests itself is by a change in propagation speed. Figure 2 illustrates some of the key issues via spatio-temporal plots of turbulent bands in a reference frame moving at the bulk velocity. Note that the imposition of periodic boundary conditions in z leads to interaction across the boundary. Figure 2a illustrates a typical long-lived turbulent band at $Re \lesssim 1000$. The band moves slowly in the positive z direction, *i.e.* downstream relative to the bulk velocity, and then decays, *i.e.* the flow relaminarizes.

Figure 2b illustrates a typical band splitting at $Re = 1100$, for which bands move upstream relative to the bulk velocity. At $t \simeq 13000$ a daughter band emerges from the downstream side of the parent band, very much like puff splitting observed in pipe flow [11, 45]. Following the split, the distance between bands decreases (from $L_z = 100$ to $L_z/2 = 50$), thereby increasing the band interaction, as can be seen by a change in the propagation velocity following the split. The time range in Fig. 2b is very long and this visually accentuates the speed change. Figure 2c presents a band splitting in a box of size $L_z = 50$ at $Re = 1200$ and shows a more pronounced difference in propagation velocities between the single band and its two offspring. The quasi-laminar gap separating the two offspring bands is quite narrow and hence the bands can be assumed to strongly interact. The spatio-temporal diagrams of Fig. 2 also show that the size of turbulent bands increases slightly with Re , and moreover that fluctuations in the size and propagation speed become greater. Fluctuations are more pronounced on the downstream side of bands.

More quantitatively, we have measured the propagation speed, U_{band} , of single turbulent bands over a range of Re in domains of different lengths L_z , as shown in Fig. 3. Periodic boundary conditions in z set the center-to-center interaction distance between bands to the domain length L_z . The velocities are measured over long times in order to obtain an averaged value and to smooth the effects of fluctuations: for $Re \in [870, 1100]$, the measurement time is taken larger than 10^4 , and for Re outside of this interval, we use the longest simulation times available (before band decay or band splitting discussed in Sec. IV and V.)

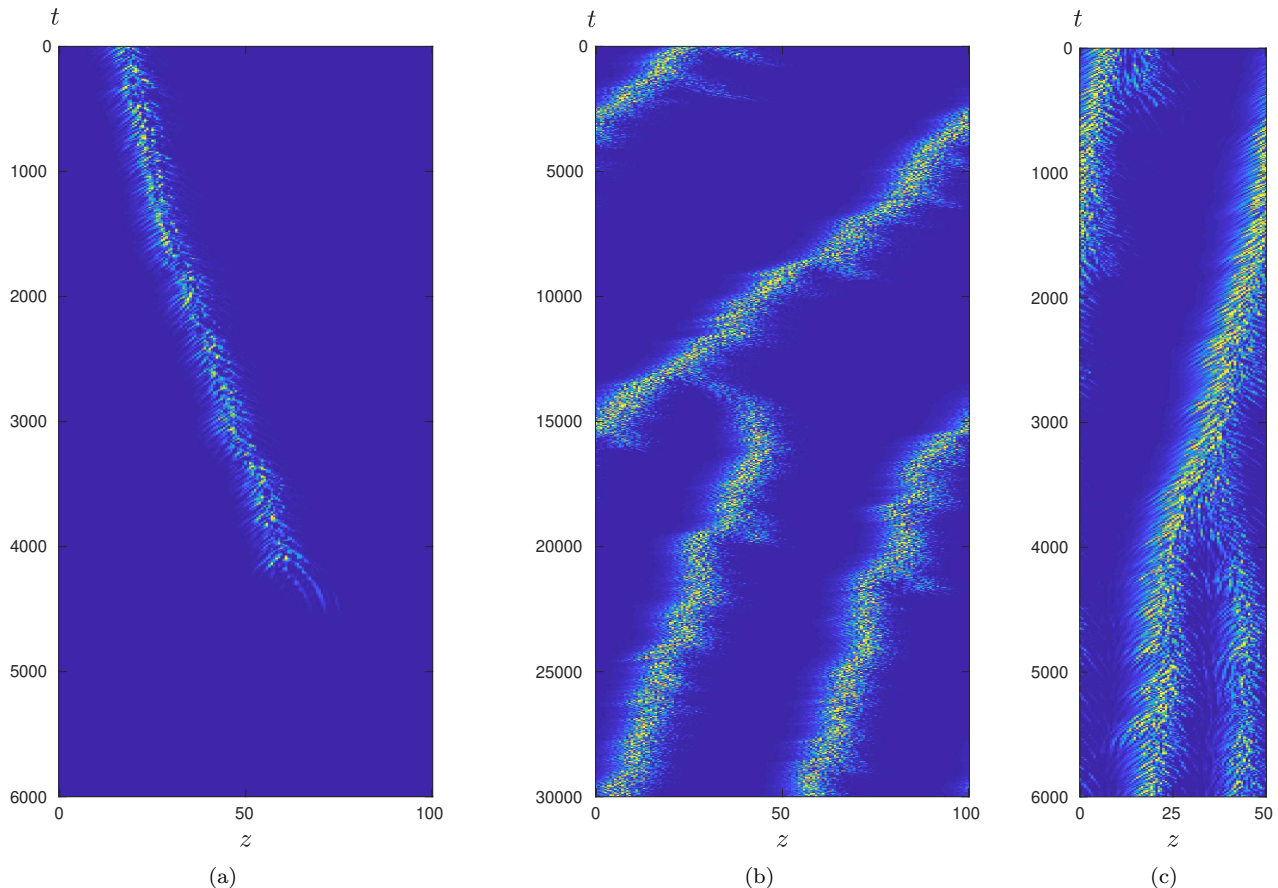


FIG. 2: Space-time diagrams of turbulent bands in a frame moving at the bulk velocity, U_{bulk} , with (a) $Re = 830$, $L_z = 100$, (b) $Re = 1100$, $L_z = 100$, (c) $Re = 1200$, $L_z = 50$. Colors show the perturbation energy $E = \frac{1}{2}(u^2 + v^2 + w^2)$ as a function of z and t , sampled in the $y = -0.8$ plane at an arbitrary value of x (yellow: $E = 0.1$, blue: $E = 0$). Average band propagation velocities, relative to U_{bulk} , and the degree of fluctuations can be discerned from diagrams. Case (a) is an example of a band moving downstream relative to U_{bulk} , which occurs for $Re \lesssim 1000$, $L_z \geq 100$, and then decaying. In case (b), a single band in a domain with $L_z = 100$ splits into two bands, resulting in a pair of bands separated in z by distance $50 = L_z/2$. The change in velocity resulting from a decrease in interaction distance is evident. Note, however, that the time range covered in the plot is large, which visually accentuates the effect. Case (c) shows band splitting in a domain of size $L_z = 50$. The resulting bands are closely spaced and interact strongly.

We find that the band speed becomes independent of L_z for $L_z \geq 100$. The speeds vary approximately linearly with Re , over the range studied, and remain close to the bulk velocity: $|U_{\text{band}} - U_{\text{bulk}}|$ is less than 2% of U_{bulk} . For values of $L_z < 100$, speeds are shifted upwards. Note that bands at $L_z = 25$ are not sustained for $Re \lesssim 1050$. Values at $L_z = 40$ are similar to those reported in a domain of the same size in [32]; Figure 3 shows that this inter-band separation is too small to be in the asymptotic regime.

We also compare the kinetic energy profile in z of stationary single bands at $Re = 1000$, calculated in domains with L_z between 50 and 200. Figure 4a shows the kinetic energy, i.e. the deviation from laminar flow, averaged over x , y , and $\Delta T = 10$, as a function of z , centered at $z = 100$. We see a strong peak and width that, except for $L_z = 50$, are nearly independent of L_z . The logarithmic representation of Fig. 4b highlights the weak tails of the turbulent bands. Except for $L_z = 50$, all have an upstream "shoulder", i.e. a change in curvature followed by a plateau. All have a downstream minimum, whose position depends on L_z : for $L_z = 50$ and 100, it is located halfway from the peak to its periodic repetition; for $L_z > 100$ the ratio of this distance to L_z decreases with increasing L_z .

Notwithstanding the long-range weak tails in Fig. 4b, we believe that turbulent bands in domains of at least $L_z = 100$ can be considered as isolated: the quasi-laminar gap is sufficiently wide that one band does not substantially affect its neighbor and modify its velocity. This seems consistent with the fact that the minimum in the z energy profile

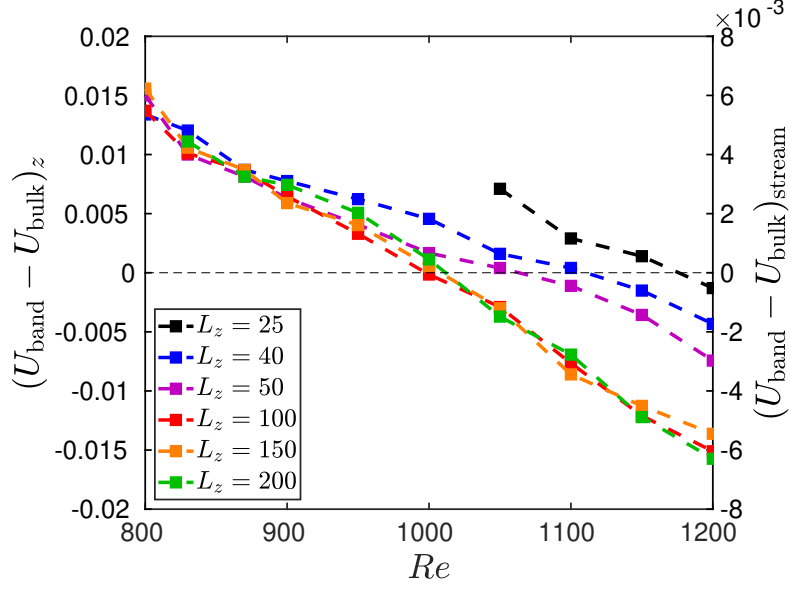


FIG. 3: Dependence of the band propagation velocity on the Reynolds number and on the inter-band distance L_z (left axis: z velocity, right axis: streamwise velocity).

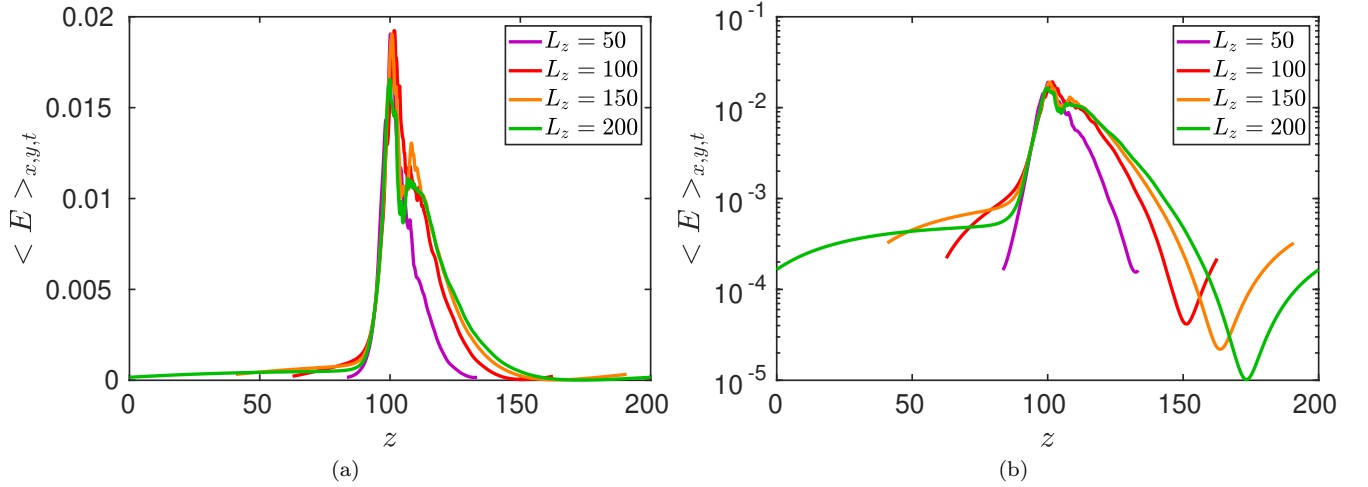


FIG. 4: Energy averaged over x , y and t as a function of z , for different L_z , in (a) linear and (b) logarithmic scales, for a one-band state at $Re = 1000$

deviates from the half-band position.

IV. ANALYSIS OF DECAY AND SPLITTING

A. Decay

We now focus on the decay and splitting events. Figure 5 illustrates a typical decay event, a turbulent band at $Re = 830$ that persists as a long-lived metastable state before abruptly decaying to laminar flow. A visualisation of the x velocity is shown in the $y = -0.8$ plane, approximately where the streaks are most intense, at representative times during the final decay to laminar flow.

States can also be characterized via their (x, z) Fourier spectra. Figure 6 shows an example of such a 2D Fourier spectrum of the x velocity at $y = -0.8$. We observe that the amplitudes along horizontal lines $m_x = 0$ and $m_x = \pm 1$ are much larger than the others. For brevity, we use \hat{u}_{m_x, m_z} to denote the modulus of the 2D Fourier component

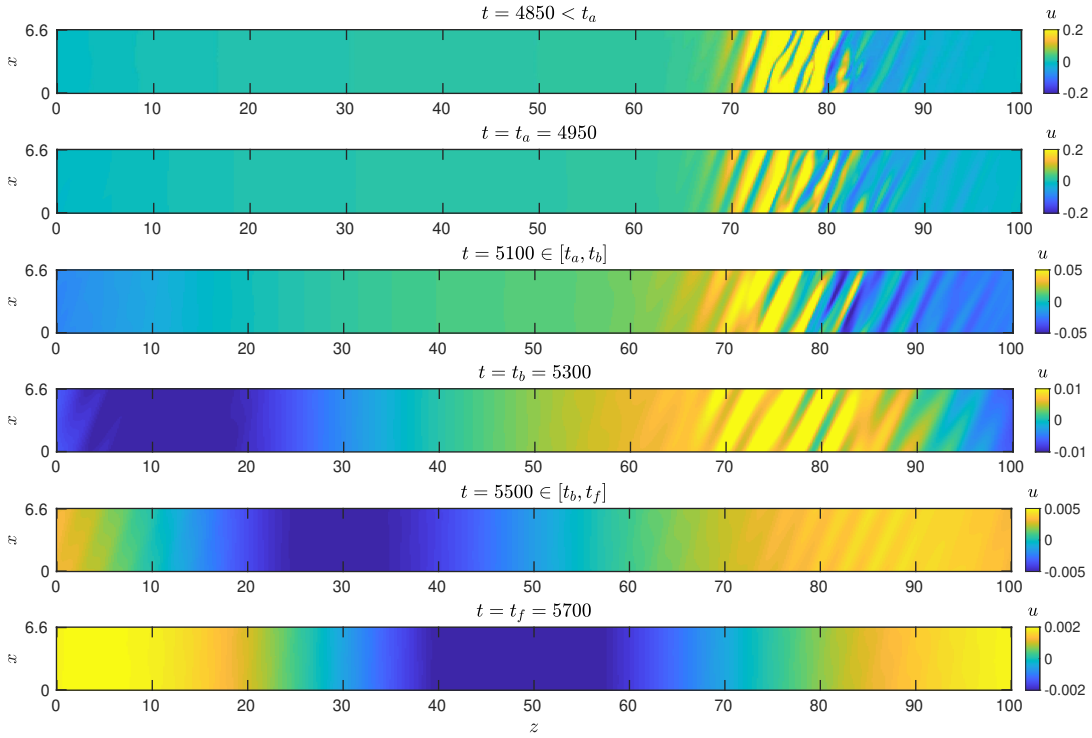


FIG. 5: (x, z) slices of x velocity at $y = -0.8$ during a band decay at $Re = 830$. Color scale represents u and changes at each time for clarity.

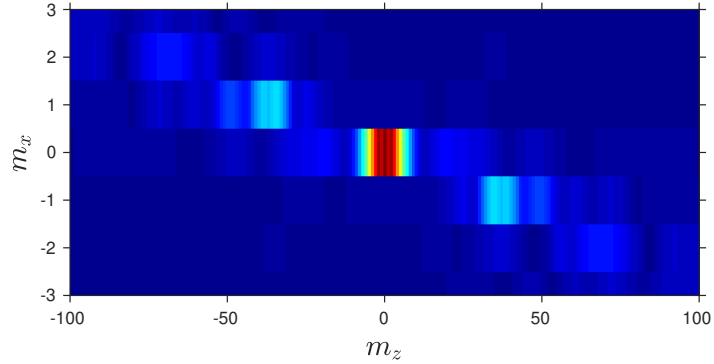


FIG. 6: Example of a (x, z) Fourier spectrum of u at $y = -0.8$, for a turbulent band at $Re = 830$. Colors show the modulus of spectral coefficients, spanning from 0 (blue) to 0.02 (red). The modulus of components $(m_x, -m_z)$ and $(-m_x, m_z)$ are equal since the velocity is real.

$(\pm m_x, \mp m_z)$ of the x velocity evaluated at $y = -0.8$. The large-scale pattern for a single band is characterized by the x -constant and z -trigonometric Fourier coefficient $\hat{u}_{0,1}$. Streaks are the small-scale spanwise variation of the streamwise velocity. Here we use the x -trigonometric Fourier coefficients of the x -velocity as a proxy for streak amplitude:

$$\hat{u}_{\text{streaks}} = \sum_{m_z=0}^{100} \hat{u}_{1,m_z}$$

Figure 7 illustrates the spectra before the beginning ($t_a = 4950$) and at the end of the decay process ($t_f = 5700$). The remaining flow field is entirely contained in the trigonometric $\hat{u}_{0,1}$ coefficient at t_f . Weak streaks are still visible but their amplitudes are 10^{-3} that of the large-scale flow $\hat{u}_{0,1}$. This shows that the transition from a turbulent band

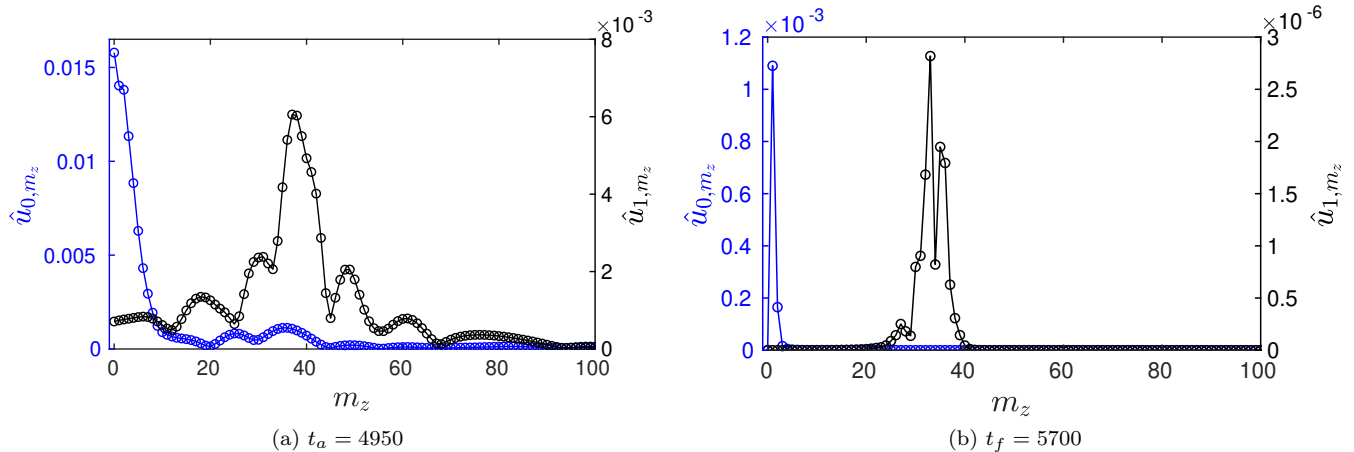


FIG. 7: Comparison between Fourier spectra \hat{u}_{0,m_z} and \hat{u}_{1,m_z} (a) before and (b) after decaying. $Re = 830$.

to the laminar state selects a large-scale flow structure aligned with the disappearing band, and moving parallel to the band. This large-scale flow, although weak and declining during laminarization, dominates the streak patterns characterizing turbulence.

Figure 8 plots the evolution in time of the spectral quantities and velocity norms. The life of the band is characterized by seemingly random oscillations of the spectral quantities and the velocity norms, especially \hat{u}_{streaks} , which shows the strongest variability. After time $t = t_a = 4950$, all the signals suddenly undergo an exponential drop, with $\|u\|_2$ and $\hat{u}_{0,1}$ decaying more slowly than $\|w\|_2$, $\|v\|_2$ and \hat{u}_{streaks} .

After the decay process is triggered, the averaged absolute level of the streaks \hat{u}_{streaks} balances the one-band structure $\hat{u}_{0,1}$ at time $t = t_b = 5300$. From this point, as \hat{u}_{streaks} and $\hat{u}_{0,1}$ have different decay rates, the one-band structure becomes prominent in comparison with the streaks. One sees indeed on the physical slices of Fig. 5 that the remaining weak flow consists primarily of a L_z -periodic structure, constant over x , and moving parallel to the previous band. Band-orthogonal and cross-channel velocities w and v are negligible in comparison to u , and only show a remaining streaky pattern, as shown on Fig. 8b.

We now consider how these quantities vary for different decay events. Figure 9 presents the evolution of spectral quantities and velocity field norms for 10 decay events. For each realization i , time is translated so that all realizations end at the same time: $t^* = t - t_{f,i} - \min(t_{f,i})$. Quantities are also normalized to obtain the same final value: $q^* = \min(q_{f,i}) \times q_i / q_{f,i}$. Note that the final time for the simulation is dictated by the criterion $\|u\|_2 < 5 \times 10^{-3}$ and that $\|u\|_2$ is dominated by $\hat{u}_{0,1}$, which is why both signals terminate with the same final value for each realization.

The evolution of the spectral component $\hat{u}_{0,1}(t)$ for the different realizations all eventually collapse onto a single curve. The same is true, slightly later, for $\hat{u}_{0,2}(t)$. The difference in decay rates for these two large-scale components is likely to be due to different shapes of the cross-channel structures.

The norm $\|u\|_2$ also behaves in this way, since it is dominated by $\hat{u}_{0,1}$, but $\|v\|_2$ and $\|w\|_2$ do not. These are sums over different spectral components each with its own decay rate, and the levels of these components differ from one realization to the next, thereby leading to different decay rates for each realization.

B. Splitting

A splitting event at $Re = 1200$ is illustrated in Fig. 10 via the evolution of (x, z) slices of u , at times from t_0 (initial band) to t_5 . The band at $t_1 = 4300$ is wider than it is at $t_0 = 3500$. Between t_1 and t_2 , the band seems to stretch. Then, a gap opens at $t_2 = 4600$, leaving a weakly perturbed turbulent-laminar interface between $z = 70$ and 80 , corresponding to the birth of the second band. The parent band continues to move towards lower z while the child band remains at its position and grows from t_2 to t_5 , smoothly acquiring all the characteristics of the parent band: a first laminar-turbulent interface composed of intense small streaks, followed by a series of wavy streaks spanning over $20h$ in z , and a second turbulent-laminar interface composed of weak straight streaks, which show a periodicity of 2 in z .

Figure 11 shows a comparison between Fourier spectra \hat{u}_{0,m_z} and \hat{u}_{1,m_z} before and after the splitting. The decrease in $\hat{u}_{0,1}$ and increase in $\hat{u}_{0,2}$, already seen in Fig. 12b, appears clearly. In addition, the two-band streak spectrum $\hat{u}_{1,m}$ shows conspicuous small-scale oscillations due to the $L_z/2$ -periodic structure, which selects even modes.

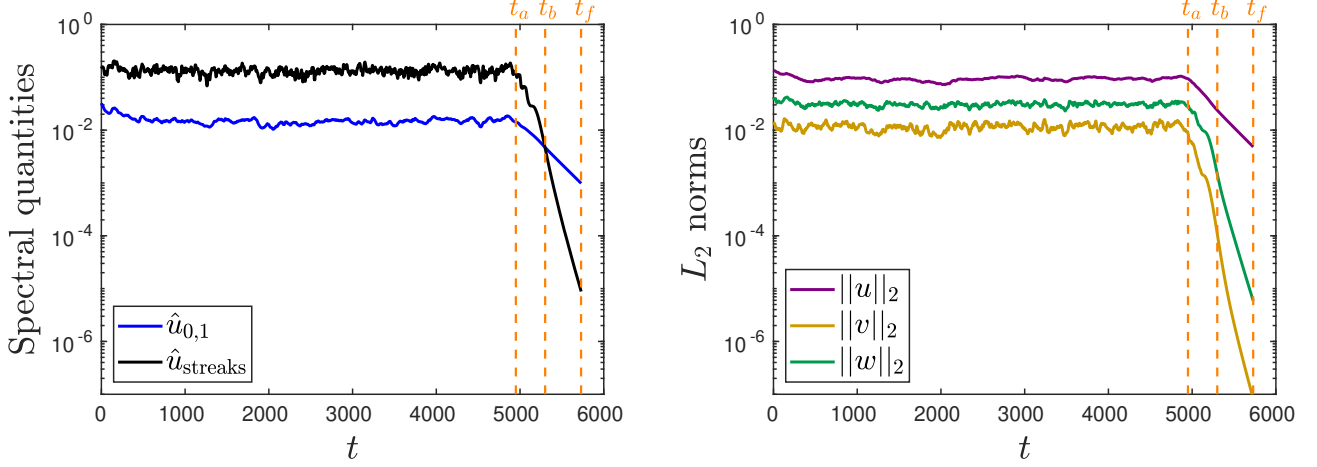


FIG. 8: Time evolution of (a) spectral quantities $\hat{u}_{0,1}$ and \hat{u}_{streaks} , (b) L_2 norms $\|u\|_2$, $\|v\|_2$ and $\|w\|_2$ for a decay event at $Re = 830$.

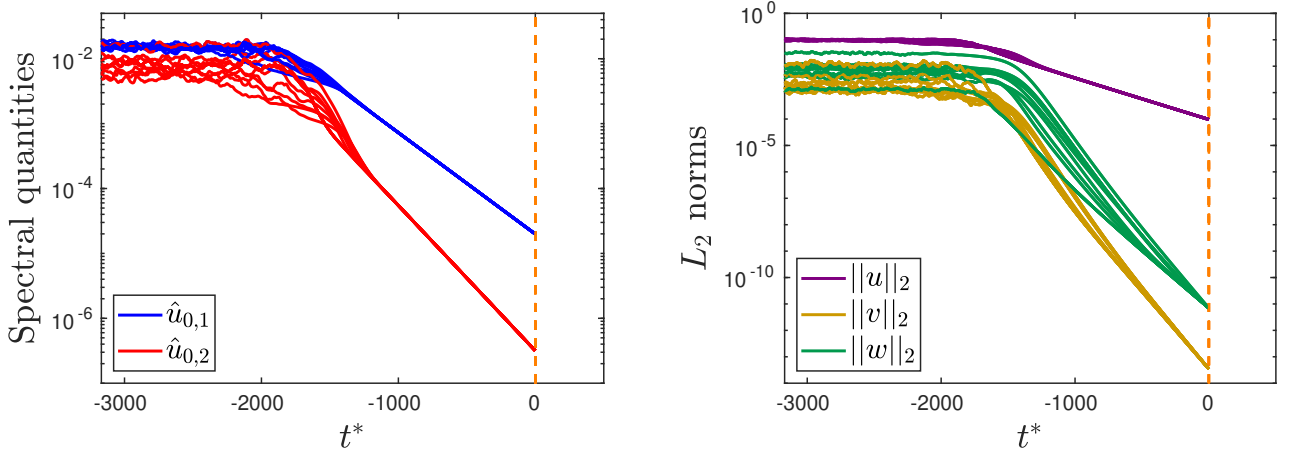


FIG. 9: Time evolution of (a) $\hat{u}_{0,1}$ and $\hat{u}_{0,2}$ and of (b) $\|u\|_2$, $\|v\|_2$ and $\|w\|_2$ during ten realizations of decay events at $Re = 830$. Time t^* and vertical quantities are respectively translated and scaled to obtain the same final value for each realization. Final decay rates for $\hat{u}_{0,1}$ and $\hat{u}_{0,2}$ (a) are -3.6×10^{-3} and -5.2×10^{-3} , respectively.

Figure 12 presents a spatio(z)-temporal diagram of the perturbation energy and traces the evolution of spectral quantities $\hat{u}_{0,1}$ and $\hat{u}_{0,2}$ at $y = -0.8$, which represent a single or a double banded pattern. The evolution of \hat{u}_{streaks} and of the L_2 -norm $\|w\|_2$ are also shown. A slight initial drop in the two-band coefficient $\hat{u}_{0,2}$ is seen from $t = t_1 = 4300$, which coincides with the appearance of the second band. A laminar gap opens between the initial band and its offspring at $t = t_2 = 4600$. Then $\hat{u}_{0,2}$ starts to increase whereas $\hat{u}_{0,1}$ decreases, from $t = t_3 = 5200$. The two quantities cross at $t = t_4 = 5600$ and finally reach plateaus at $t = t_5 = 6000$. This is the time from which the energy of the second band reaches approximately the same level as that of the first band, as seen from the spatio-temporal diagram (Fig. 12a). The other quantities, \hat{u}_{streaks} and $\|w\|_2$, follow slightly different trends from those of the spectral coefficients, as shown on Fig. 12c and 12d. Oscillations in \hat{u}_{streaks} are strong and it is difficult to distinguish trends corresponding to the band evolution. However, there is a relatively strong increase in the streak intensity just before t_5 , when the second band is fully developed. In addition, $\|w\|_2$ increases from t_1 to t_3 and then reaches a plateau of around 0.06.

The evolution before the splitting shows a missed splitting event between $t = 200$ and 1000. A weakly turbulent patch detaches from the initial stripe, and quantities $\hat{u}_{0,1}$, $\hat{u}_{0,2}$, \hat{u}_{streaks} , and $\|w\|_2$ all follow a trend between $t = 200$ and 600 similar to that between t_2 and t_3 . The birth ceases after $t = 1000$: $\hat{u}_{0,2}$ does not increase sufficiently to cross $\hat{u}_{0,1}$, and \hat{u}_{streaks} and $\|w\|_2$ drop to their previous levels.

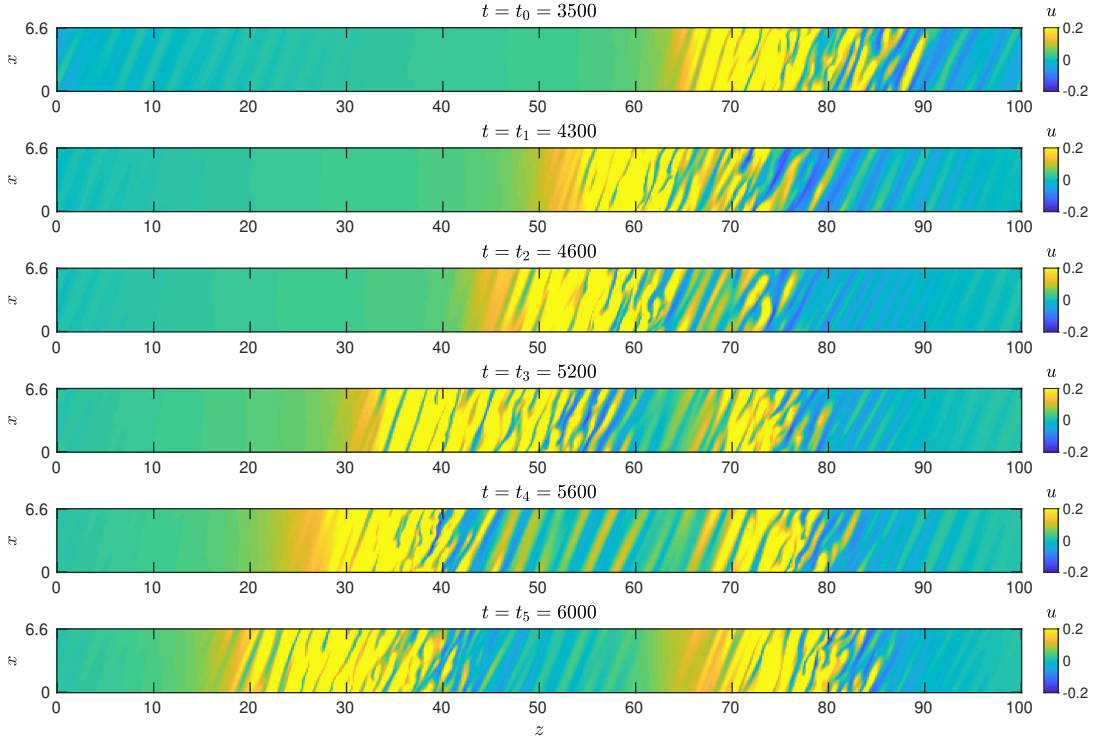


FIG. 10: (x, z) slices of x velocity at $y = -0.8$ during a band splitting at $Re = 1200$.

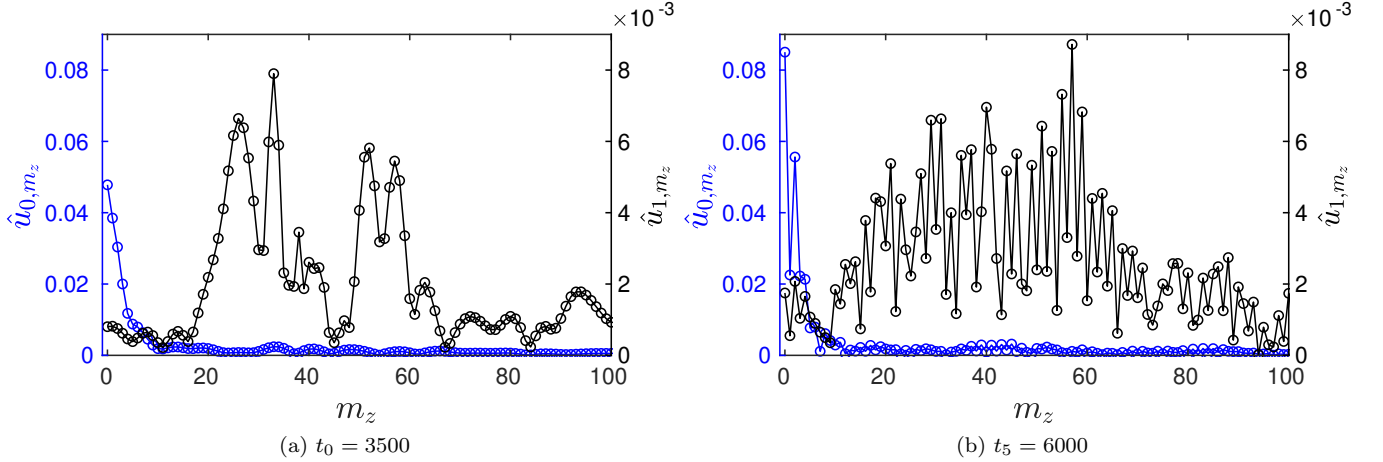


FIG. 11: Comparison between Fourier spectra \hat{u}_{0,m_z} and \hat{u}_{1,m_z} (a) before and (b) after splitting. $Re = 1200$.

We now carry out simulations in a shorter tilted domain of length $L_z = 50$ to avoid secondary splittings which would lead to a three-band state. All realizations of the formation of the second band follow the same sequence of events: an initial decrease in $\hat{u}_{0,2}$, followed by a surge in $\hat{u}_{0,2}$ while $\hat{u}_{0,1}$ drops, leading to an inversion of the dominant spectral coefficient. Meanwhile, the three-band component $\hat{u}_{0,3}$ can also be monitored to analyze the interactions between modes 1 and 2 during the splitting.

This evolution is represented in a phase portrait $(\hat{u}_{0,1}, \hat{u}_{0,2}, \hat{u}_{0,3})$ in Fig. 13. The one-band state is here characterized by an average segment around which the spectral components show noisy oscillations (state 1). Components $\hat{u}_{0,2}$ and $\hat{u}_{0,3}$ are linearly correlated to $\hat{u}_{0,1}$. $\hat{u}_{0,2}$ was already seen to be proportional to $\hat{u}_{0,1}$, as illustrated on Fig. 12b during the one-band phase during $2000 \leq t \leq 4300$. During the transition to the two-band state (state 2), $\hat{u}_{0,3}$ attains a maximum before reaching a lower value than that in state 1. The two-band state selects the even components (see Fig. 11b), therefore $\hat{u}_{0,1}$ and $\hat{u}_{0,3}$ have low values and show no correlation with the prominent $\hat{u}_{0,2}$. This representation

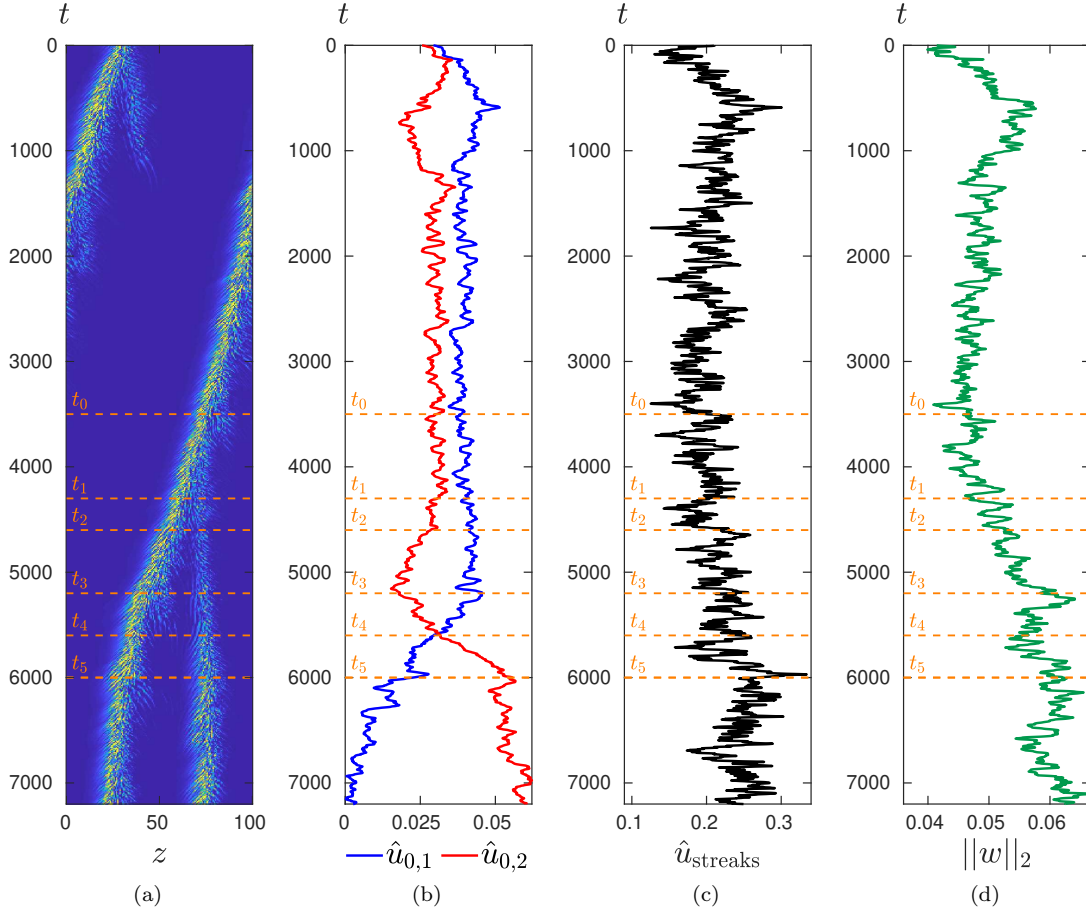


FIG. 12: Evolution of a band while it splits at $Re = 1200$. (a) Time-space diagram of the band. Colors show the turbulent perturbation energy E between 0 (blue) and 0.1 (yellow). (b, c, d) Time evolution of spectral quantities $\hat{u}_{0,1}$ and $\hat{u}_{0,2}$ (b), \hat{u}_{streaks} (c) and the L_2 -norm $\|w\|_2$ (d).

shows that large-scale spectral components statistically follow the same transition path from one to two turbulent bands.

V. STATISTICS OF BAND DECAY AND SPLITTING

We now investigate the decay and splitting statistics of single turbulent bands over a range of Reynolds numbers. The primary goal is to determine where the mean lifetimes associated with these events cross. The domain size is fixed at $L_z = 100$. Since decay and splitting events are effectively statistical, many realisations are necessary to determine the mean decay and splitting times. To generate large numbers of initial conditions for these realisations, we start from featureless turbulent flow at $Re = 1500$ and reduce Re to an intermediate value in $[900, 1050]$, where a single band then forms. We continue these simulations and extract snapshots, that are then used as initial conditions for simulations with $Re \in [700, 1350]$.

Each simulation is run with a predefined maximum cut-off time $t_f = 10^5$. If a decay or splitting event occurs before t_f , the run is automatically terminated after the event and the time is recorded. For a decay, the termination criterion is $\|\mathbf{u}\|_{L_2} < 0.005$, meaning that the flow has nearly reached the laminar base flow. For splitting, termination occurs when two (or more) well-defined turbulent zones (whose x and short-time averaged turbulent energy exceed 0.005) coexist over more than 2000 time units. We can then estimate the real time at which the splitting event occurs, defined as the time at which a second laminar gap appears from the initial band, through careful observations of space-time diagrams.

For a given value of Re , let N^d , N^s , and N be the number of decay events, splitting events, and the total number of runs, respectively. Thus $N - N^d - N^s$ is the number of runs reaching the cut-off time t_f without having decayed

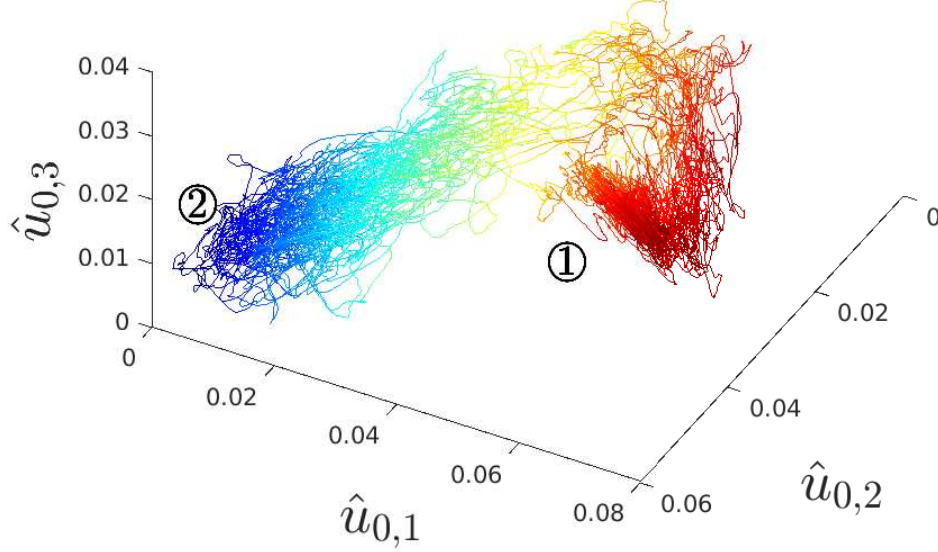


FIG. 13: Evolution of spectral quantities during 10 splittings at $Re = 1200$, in a domain of length $L_z = 50$. Each line stands for one simulation, and is colored by $\hat{u}_{0,1}$ to illustrate the transition between a one-band (1) to a two-band attractor (2).

or split.

We consider first the decay statistics. (The splitting statistics follow similarly.) The analysis follows closely previous works; see especially [11, 33, 46]. The decay times at a given Re are sorted in increasing order giving the sequence $\{t_i^d\}_{1 \leq i \leq N^d}$. The survival probability that a band has not decayed by time t_i^d is then approximated by:

$$P(t_i^d) = P(\text{decay at } t \geq t_i^d) = 1 - (i - 1)/N. \quad (3)$$

The survival distributions for decay events over a range of Re are plotted on semi-log axes in Fig. 14. The data support exponential form $P(t_i^d) = \exp(-(t_i^d - t_0^d)/\tau^d(Re))$, where $\tau^d(Re)$ is the Reynolds-number-dependent mean lifetime (characteristic time) for decay and t_0^d is an offset time. These exponential survival distributions are indicative of an effectively memoryless process, as has been frequently observed for turbulent decay in transitional flows [6, 46–50].

Quantitatively, the characteristic time $\tau^d(Re)$ is obtained by the following Maximum Likelihood Estimator [46]:

$$\tau^d \simeq \frac{1}{N'^d} \left(\sum_{t_i^d > t_0^d} (t_i^d - t_0^d) + (N - N^d)(t_f - t_0^d) \right) \quad (4)$$

where N'^d is the number of decay events larger than t_0^d . The offset time t_0^d is included to account for the time necessary for the flow to equilibrate following a change in Re associated with the initial condition, and also the fixed time it takes for the flow to achieve the termination condition after it commences decay (as seen in Fig. 8b). As in [46], we determine the value of t_0^d by varying it in Eq. (4), monitoring the resulting characteristic time τ^d , and choosing t_0^d to be the minimal time for which the estimate τ^d not longer significantly depends on t_0^d . We find $t_0^d = 850$ is a good value over the range of Re investigated.

The same procedure has been applied to the splitting events. The splitting times are denoted $\{t_i^s\}_{1 \leq i \leq N^s}$, the estimated mean lifetimes are denoted τ^s , and the offset time is denoted t_0^s . In the case of splitting we find the offset time to be $t_0^s = 500$, except for $Re = 1350$, the largest value studied. The survival distributions for various Re are plotted in Fig. 15 with $t_0^s = 500$ in all cases. With the exception of $Re = 1350$, the survival plots are again consistent with exponential distributions. The survival distribution at $Re = 1350$ deviates slightly, but distinctly, from exponential at early times. By choosing $t_0^s > 500$ for this case it is possible to obtain a more nearly exponential distribution, but we have opted to plot all data with the same value of t_0^s to highlight that at $Re = 1350$, and above, the splitting dynamics may be deviating from a memoryless process. It should be noted that obtaining splitting times becomes delicate at $Re = 1350$ because turbulence spreads in less distinct bands.

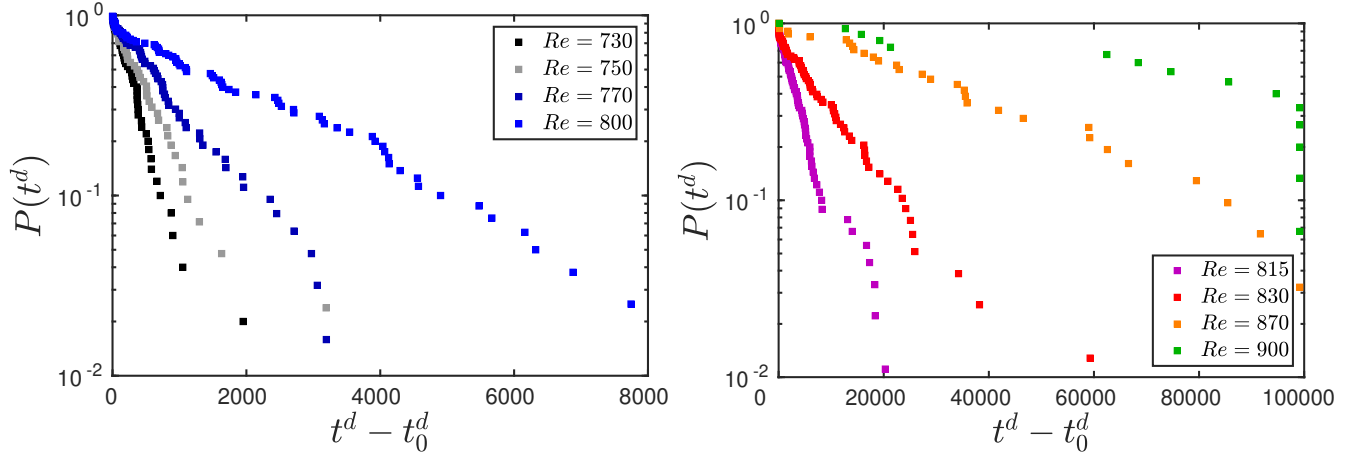


FIG. 14: Survival probability distributions of decays of a single turbulent stripe, $Re \in [730, 900]$.

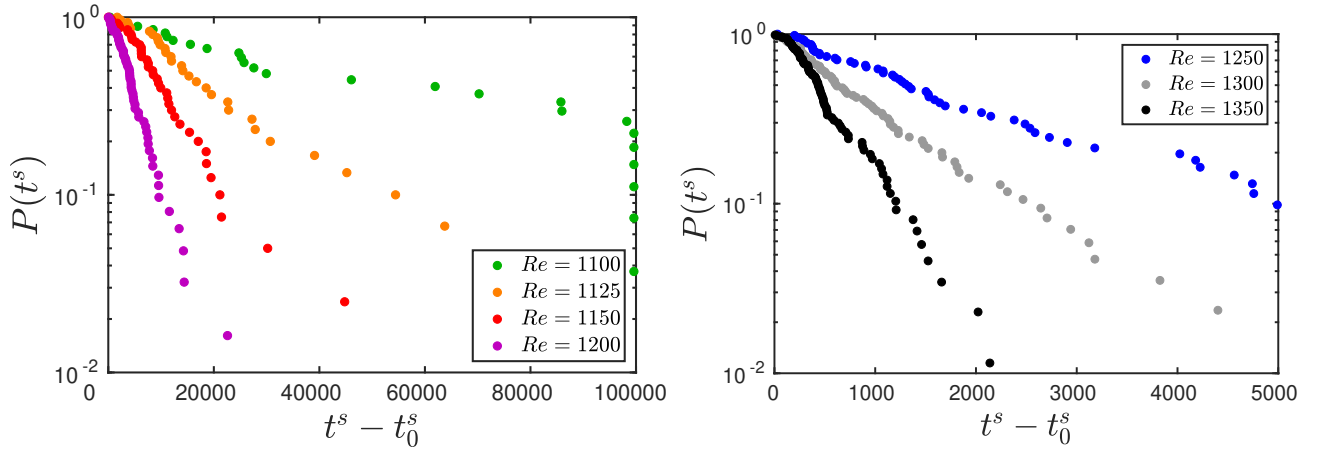


FIG. 15: Survival probability distributions of splittings of a single turbulent stripe, $Re \in [1100, 1350]$.

At $Re = 900$ and $Re = 1100$, some of the runs reach the cut-off time $t_f = 10^5$. From of a total simulation time of about 10^6 time units, we registered only 10 decay events at $Re = 900$ and 25 splitting events at $Re = 1100$, immediately showing that the characteristic lifetimes at these values of Re are respectively on the order of 10^5 for $Re = 900$, 6×10^4 for $Re = 1100$. Investigations at $Re = 950$, 1000 and 1050 were performed, but no events occurred before 10^5 time units. Due to the high numerical cost of resolving the longer time scales, we did not attempt further investigation between $Re = 900$ and $Re = 1100$. As a result, we observed no case in which both splitting and decay events occurred at the same Reynolds number, unlike for plane Couette flow [33].

Figure 16 shows the estimated mean lifetimes τ^d and τ^s as a function of Reynolds number. The error bars correspond to 95% confidence intervals for the statistical lifetime law of Type-II [51]. For $Re = 1350$ we show both the mean lifetime τ^s for full set of data plotted in Fig. 16, i.e. including the non-exponential part of the distribution, and τ^s based only on the exponential tail of the distribution using $t_0^s = 800$.

The decay lifetimes increase rapidly as a function of Re , while the splitting times decrease rapidly as a function of Re . It is clear from the main semi-log plot that both dependencies are faster than exponential. While it is not possible to conclude with certainty the functional form of the dependence on Re , the data are consistent with a double-exponential form, as shown in the inset where the double log of the lifetimes are plotted as a function of Re . The linear fits indicated in the inset are plotted as dashed curves in the main figure. From these curves one can estimate the crossing point to be $Re_{\text{cross}} \simeq 950$ with a corresponding time-scale of about 3×10^6 . The extrapolation of the data means that these values are only approximate. Nevertheless, we can be sure that the timescale of the crossing in our case is significantly above the crossing timescale of about 2×10^4 found in a similar study of plane Couette flow [33], and it appears to be about a factor of 10 less than the value 2×10^7 found for pipe flow [11].

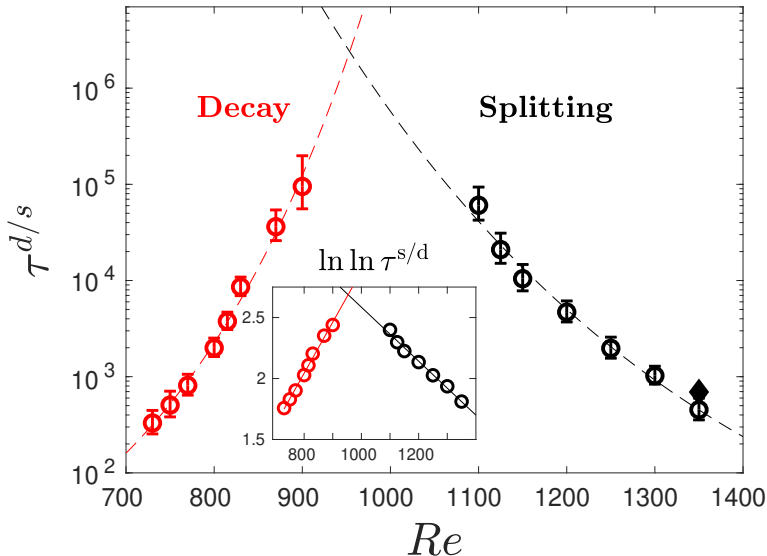


FIG. 16: Evolution of mean decay times (red) and splitting times (black) with Reynolds number Re . The error bars correspond to 95% confidence intervals. The colored black diamond corresponds to the estimated time scale at $Re = 1350$ including the non-exponential part of the distribution. Inset: $\ln \ln \tau^{s/d}$ versus Re and associated linear fits. The crossing point is at $Re_{\text{cross}} \approx 950$, $\tau \approx 3 \times 10^6$.

VI. DISCUSSION AND CONCLUSION

We have studied the behavior of oblique turbulent bands in plane channel flow using narrow tilted computational domains. Bands in such domains have fixed angle with respect to the streamwise direction and are effectively infinitely long, with no large-scale variation along the band. We have measured the propagation velocity of these bands as a function of Reynolds number and inter-band spacing and found that band speed is affected by band spacing at greater distances than previously assumed [32].

After long times, bands either decay to laminar flow or else split into two bands. Survival distributions obtained from many realizations of these events confirm that both processes are memoryless in most cases, with associated characteristic lifetimes $\tau^d(Re)$ and $\tau^s(Re)$. The dependence of these lifetimes on Re is super-exponential and consistent with a double-exponential scaling. Fitting the data with double-exponential forms, we estimate that the lifetimes cross at $Re_{\text{cross}} \simeq 950$, at about 3×10^6 advective time units. Below Re_{cross} , isolated bands decay at a faster rate than they split, while above Re_{cross} , isolated bands split at a faster rate than they decay. Hence Re_{cross} is very close to the critical point above which turbulence would be sustained in the tilted computational domain.

The characteristic times $\tau^d(Re)$ and $\tau^s(Re)$ in plane channel flow are considerably larger than those for plane Couette flow in a similar computational domain by Shi et al. [33], who found that splitting and decay lifetimes cross at about 2×10^4 advective time units. Time scales in plane channel flow are closer to those in pipe flow, where Avila et al. [11] found that lifetimes cross at about 2×10^7 advective time units. The longer lifetimes in plane channel and pipe flow, in contrast to Couette flow, could stem from higher shear rates near the walls, which could better sustain the turbulent banded state.

We also note that turbulent puffs in both pipe flow [12, 52] and channel flow move slightly faster than the bulk flow for low Re and slightly slower for high Re ; in both flows, the propagation speed becomes equal to U_{bulk} at a Reynolds number close to the critical point. It is possible that an explanation will be found that relates the two.

Our crossover Reynolds number $Re_{\text{cross}} \simeq 950$ is close to the 2D-DP threshold, calculated by Shimizu & Manneville [37] to be $Re_{\text{DP}} = 905$ or 984 (depending on how the pressure-driven Reynolds number is converted to a bulk Reynolds number). These authors carried out channel flow simulations in a large domain and extrapolated the turbulent fraction to zero using the 2D-DP power law. This agreement between the transition threshold obtained in a narrow tilted domain and in the full planar setting corroborates similar findings for plane Couette flow and stress-free Waleffe flow. Specifically, the decay-splitting lifetime crossing in tilted plane Couette flow was found by Shi et al. [33] to occur at $Re \simeq 325$. The transition point in the planar case is not known precisely, but it has been estimated by Bottin et al. [39, 40] and Duguet et al. [21] to be close to this value. In a truncated model of Waleffe flow, tilted domain

simulations indicate [38] that the critical point is at $Re_c \simeq 174$. The planar critical point was computed accurately by Chantry et al. [27] to be $Re_c = 173.80$. Heuristically some agreement between the two types of domains could be expected on the grounds that the onset of sustained turbulence is associated with its stabilization in a modified shear profile [13, 52, 53] and a narrow tilted domain quantitatively captures this process. Nevertheless, the very close agreement in several flows is unexplained.

In plane channel flow, the 2D-DP critical point is masked by the presence at lower Re of what Shimizu & Manneville [37] call the one-sided regime. This regime contains bands of long but finite length which grow via the production of streaks at their stronger downstream heads [18, 34–36]. This regime thus shows a strong asymmetry between the upstream and downstream directions and therefore has no counterpart in plane Couette flow. In this regime, bands eventually are all oriented in one direction, at about 45° from the streamwise direction and do not form a regular pattern. Since an essential feature of this regime is the long but finite length of the bands, it cannot be simulated using narrow tilted domains. This can be viewed as a shortcoming of the tilted domain in capturing the full dynamics of channel flow, but it also has the advantage of allowing us to study channel flow with the one-sided regime excluded.

We have described the evolution of a band in a narrow tilted domain during a decay or a splitting event via Fourier spectral decomposition. During a band decay, small-scale structures, streaks and rolls, are damped more quickly, increasing the relative prominence of the large-scale flow parallel to [14, 26, 29, 36, 37] or around [36, 37, 54, 55] a turbulent patch or band. All of our realizations have the same exponential decay rate at the end of the process.

Fourier analyses show that large-scale spectral components are correlated throughout the life of a band, but undergo opposite trends during a splitting event, due to one- and two-band interactions. By examining several realizations of band splitting, we find that the first three z -Fourier modes follow approximately the same path during the transition from one band to two bands. This characterization of the splitting pathway resembles transitions in other turbulent fluid systems, such as the barotropic jet dynamics in the atmosphere [56], where a rare-event algorithm has been applied to assess long time scales associated with infrequent events. The application to the study of turbulent bands splitting is currently under consideration.

ACKNOWLEDGMENTS

The calculations for this work were performed using high performance computing resources provided by the Grand Equipement National de Calcul Intensif at the Institut du Développement et des Ressources en Informatique Scientifique (IDRIS, CNRS) through grant A0062A01119. This work was supported by a grant from the Simons Foundation (Grant number 662985, NG). We wish to acknowledge Yohann Duguet, Pavan Kashyap, Florian Reetz and Alessia Ferraro for helpful discussions. Tao Liu, Jose-Eduardo Wesfreid and Benot Semin are also thanked for their inputs.

-
- [1] L. S. Tuckerman, M. Chantry, and D. Barkley, Patterns in wall-bounded shear flows, *Annu. Rev. Fluid Mech.* **52** (2020).
 - [2] O. Reynolds, An experimental investigation of the circumstances which determine whether the motion of water shall be direct or sinuous, and of the law of resistance in parallel channels, *Phil. Trans. R. Soc. Lond. A* **174**, 935 (1883).
 - [3] K. Takeishi, G. Kawahara, H. Wakabayashi, M. Uhlmann, and A. Pinelli, Localized turbulence structures in transitional rectangular-duct flow, *J. Fluid Mech.* **782**, 368 (2015).
 - [4] T. Ishida, Y. Duguet, and T. Tsukahara, Transitional structures in annular Poiseuille flow depending on radius ratio, *J. Fluid Mech.* **794** (2016).
 - [5] G. Lemoult, L. Shi, K. Avila, S. V. Jalikop, M. Avila, and B. Hof, Directed percolation phase transition to sustained turbulence in Couette flow, *Nature Physics* **12**, 254 (2016).
 - [6] A. Darbyshire and T. Mullin, Transition to turbulence in constant-mass-flux pipe flow, *J. Fluid Mech.* **289**, 83 (1995).
 - [7] M. Nishi, B. Ünsal, F. Durst, and G. Biswas, Laminar-to-turbulent transition of pipe flows through puffs and slugs, *J. Fluid Mech.* **614**, 425 (2008).
 - [8] C. W. van Doorne and J. Westerweel, The flow structure of a puff, *Phil. Trans. R. Soc. A* **367**, 489 (2009).
 - [9] B. Hof, A. De Lozar, M. Avila, X. Tu, and T. M. Schneider, Eliminating turbulence in spatially intermittent flows, *Science* **327**, 1491 (2010).
 - [10] D. Samanta, A. De Lozar, and B. Hof, Experimental investigation of laminar turbulent intermittency in pipe flow, *J. Fluid Mech.* **681**, 193 (2011).
 - [11] K. Avila, D. Moxey, A. de Lozar, M. Avila, D. Barkley, and B. Hof, The onset of turbulence in pipe flow, *Science* **333**, 192 (2011).
 - [12] D. Barkley, B. Song, V. Mukund, G. Lemoult, M. Avila, and B. Hof, The rise of fully turbulent flow, *Nature* **526**, 550 (2015).
 - [13] D. Barkley, Theoretical perspective on the route to turbulence in a pipe, *J. Fluid Mech.* **803**, P1 (2016).
 - [14] D. Coles and C. van Atta, Progress report on a digital experiment in spiral turbulence., *AIAA Journal* **4**, 1969 (1966).

- [15] C. D. Andereck, S. Liu, and H. L. Swinney, Flow regimes in a circular Couette system with independently rotating cylinders, *J. Fluid Mech.* **164**, 155 (1986).
- [16] S. Dong, Evidence for internal structures of spiral turbulence, *Phys. Rev. E* **80**, 067301 (2009).
- [17] A. Meseguer, F. Mellibovsky, M. Avila, and F. Marques, Instability mechanisms and transition scenarios of spiral turbulence in Taylor-Couette flow, *Phys. Rev. E* **80**, 046315 (2009).
- [18] T. Kanazawa, *Lifetime and Growing Process of Localized Turbulence in Plane Channel Flow*, Ph.D. thesis, Osaka University (2018).
- [19] P. Berghout, R. J. Dingemans, X. Zhu, R. Verzicco, R. J. Stevens, W. van Saarloos, and D. Lohse, Direct numerical simulations of spiral Taylor-Couette turbulence, *J. Fluid Mech.* **887** (2020).
- [20] A. Prigent, G. Grégoire, H. Chaté, O. Dauchot, and W. van Saarloos, Large-scale finite-wavelength modulation within turbulent shear flows, *Phys. Rev. Lett.* **89**, 014501 (2002).
- [21] Y. Duguet, P. Schlatter, and D. S. Henningson, Formation of turbulent patterns near the onset of transition in plane Couette flow, *J. Fluid Mech.* **650**, 119 (2010).
- [22] T. Tsukahara, Y. Seki, H. Kawamura, and D. Tochio, DNS of turbulent channel flow at very low Reynolds numbers (2014).
- [23] G. Brethouwer, Y. Duguet, and P. Schlatter, Turbulent-laminar coexistence in wall flows with Coriolis, buoyancy or Lorentz forces, *J. Fluid Mech.* **704**, 137 (2012).
- [24] K. Fukudome and O. Iida, Large-scale flow structure in turbulent Poiseuille flows at low-Reynolds numbers, *J. Fluid Sci. Tech.* **7**, 181 (2012).
- [25] F. Waleffe, On a self-sustaining process in shear flows, *Phys. Fluids* **9**, 883 (1997).
- [26] M. Chantry, L. S. Tuckerman, and D. Barkley, Turbulent-laminar patterns in shear flows without walls, *J. Fluid Mech.* **791**, R8 (2016).
- [27] M. Chantry, L. S. Tuckerman, and D. Barkley, Universal continuous transition to turbulence in a planar shear flow, *J. Fluid Mech.* **824**, R1 (2017).
- [28] D. Barkley and L. S. Tuckerman, Computational study of turbulent laminar patterns in Couette flow, *Phys. Rev. Lett.* **94**, 014502 (2005).
- [29] D. Barkley and L. S. Tuckerman, Mean flow of turbulent-laminar patterns in plane Couette flow, *J. Fluid Mech.* **576**, 109 (2007).
- [30] L. S. Tuckerman and D. Barkley, Patterns and dynamics in transitional plane Couette flow, *Phys. Fluids* **23**, 041301 (2011).
- [31] F. Reetz, T. Kreilos, and T. M. Schneider, Invariant solution underlying oblique stripe patterns in plane Couette flow, *Nat. Comm.* **10**, 2277 (2019).
- [32] L. S. Tuckerman, T. Kreilos, H. Schrobendorff, T. M. Schneider, and J. F. Gibson, Turbulent-laminar patterns in plane Poiseuille flow, *Phys. Fluids* **26**, 114103 (2014).
- [33] L. Shi, M. Avila, and B. Hof, Scale invariance at the onset of turbulence in Couette flow, *Phys. Rev. Lett.* **110**, 204502 (2013).
- [34] X. Xiong, J. Tao, S. Chen, and L. Brandt, Turbulent bands in plane-Poiseuille flow at moderate Reynolds numbers, *Phys. Fluids* **27**, 041702 (2015).
- [35] J. Tao, B. Eckhardt, and X. Xiong, Extended localized structures and the onset of turbulence in channel flow, *Phys. Rev. Fluids* **3**, 011902 (2018).
- [36] X. Xiao and B. Song, The growth mechanism of turbulent bands in channel flow at low Reynolds numbers, *J. Fluid Mech.* **883** (2020).
- [37] M. Shimizu and P. Manneville, Bifurcations to turbulence in transitional channel flow, *Phys. Rev. Fluids* **4**, 113903 (2019).
- [38] M. Chantry, private communication (2020).
- [39] S. Bottin and H. Chaté, Statistical analysis of the transition to turbulence in plane couette flow, *Eur. Phys. J. B* **6**, 143 (1998).
- [40] S. Bottin, F. Daviaud, P. Manneville, and O. Dauchot, Discontinuous transition to spatiotemporal intermittency in plane Couette flow, *Europhys. Lett.* **43**, 171 (1998).
- [41] J. F. Gibson, *Channelflow: A Spectral Navier-Stokes Simulator in C++*, Tech. Rep. (University of New Hampshire, 2012) see Channelflow.org.
- [42] J. Kim, P. Moin, and R. Moser, Turbulence statistics in fully developed channel flow at low Reynolds number, *J. Fluid Mech.* **177**, 133 (1987).
- [43] J. M. Hamilton, J. Kim, and F. Waleffe, Regeneration mechanisms of near-wall turbulence structures, *J. Fluid Mech.* **287**, 317 (1995).
- [44] H.-Y. Shih, *Spatial-temporal patterns in evolutionary ecology and fluid turbulence*, Ph.D. thesis, University of Illinois at Urbana-Champaign (2017).
- [45] M. Shimizu, P. Manneville, Y. Duguet, and G. Kawahara, Splitting of a turbulent puff in pipe flow, *Fluid Dyn. Res.* **46**, 061403 (2014).
- [46] M. Avila, A. P. Willis, and B. Hof, On the transient nature of localized pipe flow turbulence, *J. Fluid Mech.* **646**, 127 (2010).
- [47] H. Faisst and B. Eckhardt, Sensitive dependence on initial conditions in transition to turbulence in pipe flow, *J. Fluid Mech.* **504**, 343 (2004).
- [48] B. Hof, J. Westerweel, T. M. Schneider, and B. Eckhardt, Finite lifetime of turbulence in shear flows, *Nature* **443**, 59 (2006).
- [49] J. Peixinho and T. Mullin, Decay of turbulence in pipe flow, *Physical review letters* **96**, 094501 (2006).
- [50] A. P. Willis and R. R. Kerswell, Critical behavior in the relaminarization of localized turbulence in pipe flow, *Physical*

review letters **98**, 014501 (2007).

- [51] J. F. Lawless, *Statistical Models and Methods for Lifetime Data, Second Edition*, Wiley Series in Probability and Statistics (John Wiley & Sons, Inc., 2002).
- [52] B. Song, D. Barkley, B. Hof, and M. Avila, Speed and structure of turbulent fronts in pipe flow, *J. Fluid Mech.* **813**, 1045 (2017).
- [53] D. Barkley, Simplifying the complexity of pipe flow, *Physical Review E* **84**, 016309 (2011).
- [54] G. Lemoult, K. Gumowski, J.-L. Aider, and J. E. Wesfreid, Turbulent spots in channel flow: an experimental study, *Eur. Phys. J. E* **37**, 25 (2014).
- [55] L. Klotz, A. Pavlenko, and J. E. Wesfreid, Experimental measurements in plane Couette-Poiseuille flow: dynamics of the large and small scale flow, preprint (2020).
- [56] F. Bouchet, J. Rolland, and E. Simonnet, Rare event algorithm links transitions in turbulent flows with activated nucleations, *Phys. Rev. Lett.* **122**, 074502 (2019).